

To appear in ApJ: January 20, 2014, V781–1

# HiRes Deconvolved *Spitzer* Images of 89 Protostellar Jets and Outflows: New Data on Evolution of Outflow Morphology<sup>†</sup>

T. Velusamy<sup>1</sup>, W. D. Langer<sup>1</sup>, T. Thompson<sup>2</sup>

## ABSTRACT

To study the role of protostellar jets and outflows in the time evolution of the parent cores and the protostars, the astronomical community needs a large enough data base of infrared images of protostars at the highest spatial resolution possible, to reveal the details of their morphology. *Spitzer* provides unprecedented sensitivity in the infrared to study both the jet and outflow features, however its spatial resolution is limited by its 0.85m mirror. Here we use a high resolution deconvolution algorithm, “HiRes”, to improve the visualization of spatial morphology by enhancing resolution (to sub-arcsecond levels in the IRAC bands) and removing the contaminating sidelobes from bright sources in a sample of 89 protostellar objects. These reprocessed images are useful to detect: (i) wide angle outflow seen in scattered light; (ii) morphological details of H<sub>2</sub> emission in jets and bow shocks; and (iii) compact features in MIPS 24  $\mu$ m images as protostar/disk and atomic/ionic line emissions associated with the jets. The HiRes fits image data of such a large homogeneous sample presented here will be useful to the community in studying these protostellar objects. To illustrate the utility of this HiRes sample, we show how the opening angle of the wide angle outflows in 31 sources, all observed in the HiRes processed *Spitzer* images, correlates with age. Our data suggest a power law fit to opening angle *versus* age with an exponent of  $\sim 0.32$  and  $0.02$ , respectively for ages  $\leq 8000$  yr and  $\geq 8000$  yr.

*Subject headings:* infrared: ISM — stars: protostars — stars: formation — ISM: jets and outflows

---

<sup>†</sup>For fits images contact the lead author

<sup>1</sup>Jet Propulsion Laboratory, California Institute of Technology, 4800 Oak Grove Drive, Pasadena, CA 91109; velusamy@jpl.nasa.gov, William.D.Langer@jpl.nasa.gov

<sup>2</sup>1947C East Huntington Drive, Duarte, CA 91010; timthompson3@verizon.net

## 1. Introduction

Protostellar outflows and jets are believed to play a crucial role in determining the mass of the central protostar and its planet forming disk by virtue of their ability to transport energy, mass, and momentum of the surrounding material, and thus terminate the infall stage in star and disk formation. It is now well recognized that jets and outflows are essential and inherent to the star formation process and play a key role in the structure and evolution of the molecular clouds in star forming regions. The protostellar outflows are broadly classified into two types: molecular outflows traced mainly with CO emission, and jets observed by optical line emission (cf. recent reviews by Arce et al. 2007; Bally 2007; Pudritz et al. 2007). Observations indicate that around some protostars, high-velocity jets with a narrow opening angle are enclosed by a low-velocity outflow with a wide opening angle (e.g. Mundt & Fried 1983; Velusamy et al. 2007 & 2011) however, in others only one component is observed. Poorly collimated flows can be due to extreme precession of the jet (Shepherd et al. 2000) and indistinguishable from wide angle outflows. The wide angle outflows, which are also observed in the scattered light, are often missed in the optical or near-IR due to instrument insensitivity to faint emission and confusion from the bright protostellar emissions. *Spitzer* provides unprecedented sensitivity in the infrared to detect the jet/outflow features. The IRAC, IRS, and MIPS observations can provide new insight into the structure, morphology, and physical and chemical characteristics of the outflow sources as demonstrated, for example, in the observations of HH46/47 by Noriega-Crespo et al. (2004a) & Velusamy et al. (2007), Cep E by Noriega-Crespo et al. (2004b) & Velusamy et al. (2011), L1512F by Bourke et al. (2006), L1448 by Tobin et al. (2007) & Dionatos et al. (2009), L1251 by Lee et al. (2010), and HH211 by Dionatos et al. (2010). Using the IRAC colors alone, Ybarra & Lada (2009) demonstrated the feasibility to study the pure rotational H<sub>2</sub> line emissions in the shocks without the need for spectroscopic data. To get the maximum information out of the *Spitzer* images Backus et al. (2005) and Velusamy et al. (2008) developed a deconvolution program HiRes and demonstrated that resolution enhanced reprocessing of *Spitzer* images (Velusamy et al. 2007; 2011) brought out more clearly the morphologies of: (a) wide-angle outflow cavities in the IRAC 3.6 & 4.5  $\mu$ m images by scattered starlight, (b) jets and bow shocks in H<sub>2</sub> molecular emission within the IRAC bands, and (c) the hottest atomic/ionic gas in the jet head characterized by [Fe II] and [S I] line emissions within the MIPS 24  $\mu$ m band. However, to make further progress we need a large sample of objects covering protostars of different mass and luminosity and evolutionary state.

In this paper we present the deconvolved *Spitzer* IRAC and MIPS images of a large sample of 89 protostellar objects. These HiRes deconvolved images and fits image data were developed under NASA’s Astrophysics and Data Analysis Program for the purpose of mak-

ing them available to the astronomical community for further studies of these protostellar objects. The use of resolution enhanced (HiRes deconvolved) *Spitzer* images to study the morphology and properties of the protostar and its jet-outflow components has been illustrated in our earlier papers (Velusamy et al. 2007; 2011). It is not practical to discuss all the morphological details for the large sample of protostars, outflows, and jets presented here; instead, to highlight the rich detail in these HiRes images we discuss the morphology of one outflow in L1527 to reinforce the fidelity of HiRes processing and overall benefits. In addition, to illustrate how such a large data base can be useful, we use the opening angle of the wide angle outflows in our sample to discuss the possible evolution of opening angle with age. One of the outstanding issues in protostellar evolution is the role played by outflows in regulating the protostellar mass accreting process. Outflows are effective in clearing the material from the core which feed the growth of the protostar (Arce & Sargent 2006) and a widening of the outflow cavity with age can lead to termination of the infall (Velusamy & Langer 1998). The large data set here show further evidence for the opening angle to widen with age.

## 2. *Spitzer* Data and Analysis

It can be difficult to trace all the protostellar components, including the extended low surface brightness features associated with the outflow or jets, in the *Spitzer* mosaic images because these may be confused by the presence of side-lobes (Airy rings) surrounding the high brightness protostar and/or the disk. However by applying the HiRes algorithm one can minimize and at best remove the diffraction effects of the brightest features, thus enabling improved visualization of the low surface features around them. Furthermore the resolution enhancement provides a sharper view of the outflow cavity walls, molecular jets, and bow shocks.

### 2.1. Selected Jets and Outflow Sources

The sample of Class 0 protostars, H<sub>2</sub> jets, and outflow sources we selected for HiRes deconvolution of *Spitzer* images are listed in Table 1. The majority of our target protostellar objects were selected from “The Youngest Protostars” Webpage hosted by the University of Kent (<http://astro.kent.ac.uk/protostars/old/>) which are based on the young Class 0 objects compiled by Froebrich (2005). In addition to these objects our sample includes some Herbig-Haro (HH) sources and a few well known jet-outflow sources. Our sample also includes one high-mass protostar (IRAS 20126+4104; cf. Caratti o Garatti et al. 2008) to demonstrate

the use of HiRes for such sources. Our choice for target selection was primarily based on the availability of *Spitzer* images in IRAC and MIPS bands in the archives and the feasibility for reprocessing based on the published *Spitzer* images wherever available.

## 2.2. HiRes Deconvolution

To maximize the scientific return of the *Spitzer* images we use the HiRes deconvolution processing technique that makes optimal use of the spatial information in the observations. The algorithm, “HiRes” and its implementation has been discussed by Backus et al. (2005) and its performance on a variety of astrophysical sources observed by *Spitzer* is presented by Velusamy et al. (2008). The HiRes deconvolution algorithm is based on the Richardson-Lucy algorithm (Richardson 1972; Lucy 1974), and the Maximum Correlation Method employed by Aumann et al. (1990) for IRAS data. As demonstrated by Velusamy et al. (2007; 2008) the HiRes deconvolution on *Spitzer* images retains a high fidelity and preserves all the main features. HiRes deconvolution improves the visualization of spatial morphology by enhancing resolution and removing the contaminating sidelobes from bright sources. The benefits of HiRes include: (a) enhanced resolution of  $\sim 0.6'' - 0.8''$  for IRAC bands,  $\sim 1.8''$  and  $\sim 7''$  for MIPS 24  $\mu\text{m}$  and 70  $\mu\text{m}$  images, respectively; (b) the ability to detect sources below the diffraction-limited confusion level; (c) the ability to separate blended sources, and thereby provide guidance to point-source extraction procedures; and, (d) an improved ability to show the spatial morphology of resolved sources. We reprocessed the images at all the IRAC bands and the MIPS 24 and 70  $\mu\text{m}$  bands using all available map data in these bands in the *Spitzer* archives containing the selected protostellar objects.

We used the pipeline processed basic calibrated data (BCD) and post-BCD (pBCD) down-loaded from the *Spitzer* Science Center (SSC) archives. Our nominal data processing produced reprocessed images at each band by applying the HiRes deconvolution on BCDs following the steps outlined by Velusamy et al. (2008). The images containing 44 objects, as noted by “bcd” in column 7 of Table 1 were processed in this mode using BCDs as input to HiRes. All the HiRes images using the BCD images as input were obtained after 50 iterations. Though HiRes was originally designed to take BCD images as input, we have found it worked equally well when mosaic images were used (c.f. IRAS20293+3952 and IRAS05358+3843 by Kumar et al. 2010; M51 by Dumas et al. 2011). For 41 protostellar objects processed after 2012 we used the post-BCD images as input to HiRes deconvolution taking advantage of the improved data products in the *Spitzer* archives. These objects are identified in Table 1 (column 7 as “pbc”). The post-BCD data are mosaic images made using the BCD images after some re-sampling applying convolutions. Therefore in comparison to

the BCD images as input, the mosaic images represent already smoothed input images. Thus the HiRes deconvolution of such images converge more slowly, and typically requires about 150 iterations to match the same level as with BCDs as input.

The overall performance of HiRes deconvolution on the *Spitzer* images presented here is in good agreement with those in the previously published examples (c.f. Velusamy et al. 2008). The HiRes deconvolution interpolates well across the “bad” (NaNed) pixels in the input images such as due to muxbleed, and saturation. All bands are relatively free of artifacts except for the IRAC channels 3 and 4, (in particular at  $8\ \mu\text{m}$ ) which in some cases show streaks due to muxstripping and a spurious secondary component adjacent to very bright sources due to uncorrected muxbleed. Such spurious secondary components seldom occur with HiRes in the BCD input mode. However, in the post-BCD input mode our algorithm can miss muxbleed pixels because of the convolutions used in the post-BCDs. Such spurious components if present in the maps are identified in Fig. 3.1(b) to 3.53(b). A note of caution, when interpreting multiple components in the vicinity of bright objects in  $8\ \mu\text{m}$  images one should examine more closely the sources to check whether they might be artifacts in the data or are real.

The angular resolutions in the deconvolved images are typically in the range of  $0.6''$  to  $0.8''$  in IRAC bands  $3.6\ \mu\text{m}$  &  $4.5\ \mu\text{m}$ ;  $0.8''$  to  $1''$  in IRAC  $5.8\ \mu\text{m}$  &  $8\ \mu\text{m}$ ;  $\sim 2''$  and  $\sim 6''$  in MIPS  $24\ \mu\text{m}$  and  $70\ \mu\text{m}$  respectively which are a factor of 2 better than those in the mosaic images. The resolution enhancement achieved depends on the signal-to-noise-ratio, the image coverage (redundant sets of BCD or post-BCD images used as input) and the background levels for the point sources. The angular resolution in each HiRes image can be obtained by examining Gaussian fits to the “point” sources in each image.

### 3. RESULTS AND DISCUSSION

The advantages of the enhancement in the HiRes images to visualize the morphological details over the mosaic images are evident in all IRAC and MIPS bands as shown in our earlier papers (Velusamy et al. 2007; 2008; 2011). In Figures 1 and 2 we show examples of comparison between the mosaic and HiRes images to highlight the merits of HiRes deconvolution. In Figure 1 we reproduce one of the unprocessed 3-color images of *Spitzer* IRAC bands from the literature (Tobin et al. 2008) in the upper panel and show the corresponding image obtained with HiRes processing in the lower panel. The resolution enhancement is evident from the sizes of the point sources in the field and its manifestation in tracing the outflow cavity walls and the protostar environment are obvious. Figure 2 demonstrates the fidelity of the HiRes processing. Here we use the high resolution Gemini  $L'$  - band ( $3.8\ \mu\text{m}$ )

image (with a pixel scale of  $0.049''$ ) of the outflow in L1527, observed by Tobin et al. (2010) as a “truth image” for comparison with the sub-arcsec resolution IRAC  $3.6\ \mu\text{m}$  image obtained after the deconvolution. Note the vertices of the outflow lobes which are fully resolved in the Gemini  $L'$  - band image are remarkably consistent with the elongated structure in the *Spitzer* HiRes image. (The differences in the asymmetry of the brightness in the vertices may be a consequence of the scattering across the different band shapes.)

In this paper, we present in Figures 3.1 to 3.53 the results of HiRes deconvolution of *Spitzer* images containing 89 protostellar objects and associated jets and outflows. A list of the objects and maps are summarized in Table 1. These objects have been studied by several authors. The reference(s) in column 6 are provided only as examples where the basic data on the object is given. In column 7 we list the type of the input data used for HiRes processing as discussed in Section 2.2. The last column (8) lists the Figure number in which the images of the object is shown. Each HiRes image typically covers an angular size of  $\sim 5'$  and may include one or more protostellar objects or jet/outflow features as listed in Table 1 and these are identified in the respective figures Figures 3.1 to 3.53. The HiRes fits data will be available in the IRSA web site in early 2014. Our objective here is limited to presenting an overview of the deconvolved images to give a perspective on how this data could support further studies of protostellar jets and outflows. Therefore, for illustrative purposes we only discuss one image in detail.

### 3.1. HH 1-2: as an example of HiRes images

Fig 3.1 is an example of how our HiRes images are displayed in Figures 3.1 to 3.53. In each figure there are two panels: (a) the  $24\ \mu\text{m}$  emission is overlaid as contours on the  $4.5\ \mu\text{m}$  image, and (b) a RGB 3-color representation of IRAC  $3.6\ \mu\text{m}$  (blue),  $4.5\ \mu\text{m}$  (green) and  $8\ \mu\text{m}$  (red). We chose to display a  $4.5\ \mu\text{m}$  image since it traces equally well both the scattered light and  $\text{H}_2$  line emissions in the jet-outflow. The  $24\ \mu\text{m}$  emission contours identify the driving source (protostar/disk) associated with the jets and outflows. Furthermore, in cases where the atomic jet features, traced by the atomic and/or ionic line emissions within the MIPS  $24\ \mu\text{m}$  band, are present they are identified by the  $24\ \mu\text{m}$  contours overlaid on  $4.5\ \mu\text{m}$  gray scale image. To bring out such features more clearly, where it is useful, we show a blowup of the selected regions (indicated by the boxes in the left panel) on the right hand side of the figure. The 3-color representation in the lower panel (labeled (b)) helps to bring out the color differences among various features, especially the wide angle outflow traced by blue representing the scattered light (predominantly at  $3.6$  and  $4.5\ \mu\text{m}$ ) and the  $\text{H}_2$  jets/bow shocks by green and red. The protostellar object and the jet-outflow features

are also identified in the Figures in panels (a) and (b).

HH1/HH2 is a well studied system (being the first detected Herbig-Haro object), see, for example, Noriega-Crespo & Raga (2012) for detailed anatomy of jets and counter-jets as seen in *Spitzer* images. It is a good example to illustrate the significant features that can be traced in the HiRes *Spitzer* images. Furthermore, as far as we know this object is the only one for which there exists a deconvolved image using other techniques. Note that the HiRes image at  $4.5\ \mu\text{m}$  in Fig. 3.1a compares well with a recently deconvolved image (Noriega-Crespo & Raga, 2012) obtained by using a different algorithm, the deconvolution software AWAIC (A *WISE* Astronomical Image Co-Adder), developed by the Wide Field Infrared Survey Explorer (*WISE*) for the creation of their Atlas images (see, e.g., Masci & Fowler 2009). Of particular importance in our results, as seen in the enlarged view (in the right panels in Fig 3.1a) is the association of  $24\ \mu\text{m}$  features with the optical knots in HH2 (south-east) as identified by Raga et al. (1990) and Noriega-Crespo & Raga (2012) as well as with the jet and counter jet. These  $24\ \mu\text{m}$  features trace the atomic and ionic jet features as discussed in the cases of HH46/HH47 and Cep E (Velusamy et al. 2007 & 2011). Another new feature in our results in Fig 3.1b is the detection of the wide angle outflow cavity implying that the protostar HH1-2 VLA is driving simultaneous wide angle outflow and collimated jets.

As reported in the case of Cep E (Velusamy et al. 2011) the MIPS images have small pointing differences ( $\sim 1''$ ) with respect to the IRAC images. This offset is also evident in some of the maps shown Figures 3.1 to 3.53. The difference in the positions of the point sources between the IRAC and MIPS images is, in part, due to the fact that MIPS used a scan mirror to change the field of view (FOV) during their observations and the mechanism itself suffered a hysteresis effect that increased the positional uncertainty by  $0.6'' - 1.0''$ . This uncertainty is a small fraction of the MIPS beam at  $24\ \mu\text{m}$  in the mosaic images, but it becomes more obvious when comparing MIPS and IRAC HiRes images. Note that the MIPS images shown in the figures or the fits image data are not corrected for any pointing offset with respect to the IRAC images. Therefore, in case detailed positional matching is required, the pointing offset can be obtained by comparing the “point” sources in the MIPS  $24\ \mu\text{m}$  image with their counterparts in the IRAC bands using the HiRes fits images. The MIPS handbook gives a  $1-\sigma$  radial uncertainty of  $1.4''$ , in comparison with  $\sim 0.2''$  for IRAC.

One problem with HiRes deconvolution is that it tends to resolve out very smooth, extended low surface brightness features. Optimal performance HiRes requires that the background emission is fully subtracted out in each BCD prior to applying the deconvolution. Furthermore, the positivity criteria implicit in the deconvolution algorithm makes it insensitive to negative intensities. In rare cases (as in Fig. 3.53) though the HiRes decon-

volved image is free from the sidelobe contamination from bright sources in the image, its resolution enhancement and its lack of preserving the background can make it harder to detect extremely extended low surface brightness emissions.

### 3.2. Summary of *Spitzer* HiRes images

Figures 3.1 to 3.53 highlight the prominent features in the HiRes images of the protostar regions. The HiRes fits images contain more details over the full extent of the processed maps and will be available in the IRSA web site in early 2014. *Spitzer*'s coverage of a broad range of IR emissions in the IRAC and MIPS bands with high sensitivity and photometric stability along with the IRS data in some cases, provide sufficient information for a comprehensive modeling of the spectral energy distribution (SED) to derive the physical characteristics and the evolutionary stages of protostars (cf. Robitaille et al. 2007; Forbrich et al. 2010). However, by applying the HiRes re-processing we can extract even more information from the *Spitzer* data. As demonstrated in Figure 3.1 the sensitivity, the resolution enhancement and removal of the diffraction lobe confusion have led to visualizing and characterizing more clearly the following:

1. very high dynamic range in the maps in which the protostar is well resolved on a sub-arcsec scale from the surrounding jets and outflows;
2. the protostar–disk itself is detectable in the IRAC bands in many cases (with relatively low obscuration) and almost always in MIPS bands;
3. wide-angle outflow cavities in the IRAC 3.6 and 4.5  $\mu\text{m}$  images are identified by the scattered photospheric starlight; although they are visible in the Mosaic standard Post-BCD products, they are brought out more clearly in the HiRes images;
4. jets and bow shocks in  $\text{H}_2$  molecular emission within the IRAC bands; and,
5. the hottest atomic and ionic gas in the jet and jet-head traced by the  $[\text{Fe II}]/[\text{S I}]$  line emissions within MIPS 24  $\mu\text{m}$  band.

The *Spitzer* IRAC and MIPS bands offer a unique resource to study a wide range of components simultaneously: protostars, protostellar disks, outflows, protostellar envelopes and cores. At the short wavelength IRAC bands the outflow cones are observable in scattered light from the protostar through the cavity created by the jets and outflows (cf. Tobin et al. 2007; Velusamy et al. 2007; 2011). A significant fraction of the emission in the IRAC bands is also considered to contain emission from the  $\text{H}_2$  rotational lines (e.g. Noriega-Crespo et al.



2004a,b; Smith & Rosen, 2005; Neufeld & Yuan, 2008) and therefore is an excellent tracer of  $\text{H}_2$  emission in the protostellar jets. Recently Velusamy et al. (2007; 2011) have shown that molecular jets and molecular gas in the bow shocks are readily identifiable in the IRAC bands, while the hottest atomic and ionic gases in the bow shocks, are also identifiable in the MIPS 24  $\mu\text{m}$  band which covers a few atomic and ionic emission lines. The dust emission from the protostar in the MIPS bands is a good diagnostic of the circumstellar disks.

With the exception of HH 1-2 MMS 3 all the other protostars are detected in one or more bands in the processed images. In at least three cases, BHR 71, CG 30 and CB 230 we clearly detect the binary components and associated  $\text{H}_2$  jets and outflows. The binary components (A,B) in L1448 IRS3 (cf. Tobin et al. 2007), IRAS 16293-2422 (cf. Takakuwa et al. 2007) and L723 (cf. Girart et al. 2009) are marginally to well resolved in the 24  $\mu\text{m}$  HiRes images. We clearly detect 31 wide angle outflows in scattered light in the IRAC bands (there may be others that are less obvious due to confusion with other features). Out of these there are 12 outflows, including B5 IRS1 which is known to have pc scale HH flows (Yu et al. 1999) in which no detectable  $\text{H}_2$  jets or bow shocks have been observed. In about 14  $\text{H}_2$  jet/bow-shock systems the atomic/ionic emission in the jet/jet-heads are detected in the MIPS 24 $\mu\text{m}$  images. Prominent atomic jets are evident, for example, in Figs. 3.1 (HH 1-2), 3.16 (HH 211), 3.30 (HH 92), 3.31 (HH 212), 3.37 (HH 46/47) 3.42 (Serp-SMM1), and 3.52 (Cep E).

Thirty one of the wide angle outflows, representing a large fraction of the sample, show the high efficiency of the scattered light in the *Spitzer* images as a tracer of outflow cavities. In Fig. 4 we show an image gallery of all 31 outflows. Though the wide angle outflows are observed by their CO emission, a comparison between the outflow cavities traced in the *Spitzer* images of HH46 and in the ALMA maps of CO emission show that the former is broader than the latter (Arce et al. 2013). In the case of CB 26 (Launhardt et al. 2008) a narrower outflow is also detected in CO than seen in the scattered light cavity. Arce et al. argue that the narrower outflow seen in  $^{12}\text{CO}$  is a consequence of opacity effects. In Figs. 5 and 6 we show two examples of a comparison between the *Spitzer* scattered light cavity and the CO outflows. In the case of L 483, shown in Fig. 5, we overlay the red and blue shifted  $^{12}\text{CO}$  (1-0) intensity contours on the HiRes *Spitzer* image at 4.5  $\mu\text{m}$ . The  $^{12}\text{CO}$  (1-0) maps are from our unpublished OVRO observations made in 1997. The red-shifted lobe is narrower than the blue-shifted lobe and both show narrower opening angle in comparison to that in the scattered light. The narrower opening angle for the CO outflow may be evidence for  $^{12}\text{CO}$  opacity effects close to the source. In the second example shown in Fig. 6 we compare the scattered light in the HiRes *Spitzer* image at 4.5  $\mu\text{m}$  of Cep E (left panel) with the OVRO  $^{13}\text{CO}$  (1-0) maps (right panel) obtained by Moro-Martín et al. (2001). Clearly the  $^{13}\text{CO}$  outflow seems to trace the full extent of the scattered light

cavity (also shown in Fig. 3.52) as may be expected for  $^{13}\text{CO}$  which has lower opacity compared to  $^{12}\text{CO}$  in the previous example. Thus compared to CO the *Spitzer* images offer a more powerful tool to study morphology of wide angle outflows detected in the scattered light. In addition to the scattered light cavities, the  $\text{H}_2$  molecular jets, bow shocks, and in some cases the atomic/ionic jet components when present are also detected in the *Spitzer* images thus providing a more complete morphology of the protostellar outflows and jets. The predominance of simultaneous presence of collimated jets and wide angle outflows in our sample (19 out of 31) is consistent with unified jet-outflow models such as presented by Machida et al. (2008) in which the accretion in the compact protostellar disk drives the high velocity jets and the accretion from the extended infall envelope drives the wide angle outflows.

Our sample contains a large number of  $\text{H}_2$  jet/bow shocks (partly due to selection of many known HH objects). The data presented here provide a comprehensive data base to study the number, distribution and their separation from the protostar, of the  $\text{H}_2$  knots and bow-shocks which are indicators of the episodic ejections and/or the inhomogeneities in the surrounding ISM.

### 3.3. Time evolution of outflow morphology

Protostellar jets and outflows carve cavities and inject energy, momentum and turbulence into the surrounding medium (e.g., Shu et al. 2000; Bally et al. 2007). They have a profound effect on the parent core, which is the reservoir for material accreted by the forming star and thus on the final properties of the newborn star as well. Outflows originate close to the surface of the forming star (e.g., Pudritz et al. 2007), and such clearing out of the gas and dust along with a widening of the outflow with time can lead to the termination of the infall phase (Velusamy & Langer 1998). A possible evolutionary trend in the outflow morphology (widening with time) as a function of age was seen in a sample observed in CO (Arce & Sargent, 2006) and is predicted in the simulations of outflow evolution (Offner et al. 2011). A broadening of outflow with age was also found by Seale & Looney (2008) who used the scattered light in the outflow cavities in the unprocessed *Spitzer* images of 27 YSOs combined with their SEDs to quantify the shapes of the outflow.

In Table 2 we list all the 31 wide angle outflows detected in our sample (see Fig. 4a & b) along with the opening angles measured as discussed below. The outflow shapes are typically parabolic: with the opening angles being the broadest at the base and narrower at larger distances from the vertex of the cavity. As discussed in Velusamy & Langer (1998) to study the evolution of the outflow, the opening angle measured near the base is most

relevant. When bipolar outflow is clearly seen we use only the widest lobe for measuring the opening angle. We do not use the average of the opening angles of the outflow and the counter outflow because, in addition to the evolutionary status of the outflow, its observed characteristics may vary with factors such as the viewing geometry (inclination), and/or environmental conditions of the protostellar and circumstellar envelopes. For the purpose of tracing the outflow evolution with age, the most critical outflow characteristic is the opening angle near the vertex, at the start of the outflow (c.f. Velusamy & Langer, 1998) before it is modified by any environmental effects. Therefore we can assume that the widest opening angle in any of the lobes would be the most representative of the opening angle for correlating with age. The opening angles are not corrected for inclination and are listed in column 2 of Table 2. Note that the arrows marked in Figs. 3.1(b) to 3.53(b) are meant to draw attention to the presence of wide angle outflow and they do not represent the exact opening angles. The values of the opening angles in Table 2 are measured between the boundaries of the widest outflow lobe in each object.

Following the approach of Arce & Sargent (2006) we use  $T_{bol}$  as a measure of the protostellar age. In Table 2 we list the values for  $T_{bol}$  collected from the literature as indicated in column 3. When a range of values are given we use their mean value for estimating the ages. In a few cases we estimated the  $T_{bol}$  values using the SEDs available in the literature and these are noted in the Table. The ages were estimated from  $T_{bol}$  using the empirical relationship given by Ladd et al. (1998) in Appendix Eq. C9. The ages and their uncertainty are listed in column 5 in Table 2. The uncertainty in the estimated ages corresponds to the uncertainty in the empirical fit as given by Ladd et al. In Figure 7 we show the plot of opening angle versus protostellar age for all 31 outflows in our sample (denoted by crosses). The uncertainty in the ages is also indicated. The error in the measured opening angles is small  $< 5^\circ$ . We also included in this plot the data from Arce & Sargent (2006) represented by filled triangles. The scatter in this plot is large; but a trend in the opening angle, increasing with age is evident. For example we can fit power laws as shown in Fig. 4: Opening angle,  $\theta(\text{deg}) = 6.7 \times [t(\text{yr})]^{0.32}$  for ages  $< 8000$  yr and  $\theta(\text{deg}) = 88.5 \times [t(\text{yr})]^{0.02}$  for ages  $> 7000$  yr. (For the fits we use only the data in our sample, all observed by scattered light in the processed *Spitzer* images). At ages  $\geq 8000$  yr the plot suggests a slower rate for the increase of opening angle with time, which would be consistent with the opening angles approaching  $180^\circ$  asymptotically. The scarcity of data at higher ages is due to the fact that our sample is primarily Class 0 objects with just two Class 1 objects (B5 IRS1 & HH46/47). It may be noted that we do not correct the opening angle for inclination. Though a widening trend is evident in our data any interpretation of fit to the data is subject to the large uncertainty in their ages.

Our results are broadly consistent with the plots in Arce & Sargent (2006) and Seale

& Looney (2008). However our values for the opening angles seem higher than those in their results. The “intensity weighted” opening angles estimated by Seale & Looney using azimuthal intensity in their circular cuts are also likely to be narrower than that measured geometrically on high spatial resolution images. Arce & Sargent used CO outflow data. Due to opacity effects the  $^{12}\text{CO}$  may not trace the entire extent of the outflow cavity as that traced by scattered light as seen in Fig.5 (also see Arce et al. 2013). Thus the data from the HiRes processed images clearly provide the most consistent set of apparent opening angles for the entire extent of the cavity. Nevertheless, the observed trend in the opening angle versus age is subject to the large uncertainties in estimating the ages. Reliable age estimates combined with a more detailed characterization of the morphological shape of the cavity should provide observational constraints to the theories of outflow and star formation processes.

#### 4. Summary

By combining the high sensitivity of *Spitzer* images and reprocessing with HiRes deconvolution on a large sample of protostellar objects, we show that the jet and outflow features are more easily identified than those in the *Spitzer* mosaic images alone. These features are: (i) wide angle outflow seen in the scattered light; (ii) morphological details of jet driven bow shocks and jet heads or knots; (iii) compact features in  $24\ \mu\text{m}$  image identified as atomic/ionic line emission within the MIPS band coincident with the jet features. The maps and the fits image data presented here can be used to study in detail these protostellar components as demonstrated in the case of Cep E (Velusamy et al. 2011). We can study directly the scattered light spectrum and hence the protostellar SED in deeply embedded protostars, by separating the protostellar photospheric scattered emission in the wide angle cavity from the jet emission. The high contrast resolution enhanced images in the *Spitzer* HiRes sample provide a robust description of the morphology of the wide angle outflow cavity in 31 objects. A trend for the widening of the opening angle with age is evident in the power law fits to this data. We can obtain the  $\text{H}_2$  emission line spectra as observed in all IRAC bands for the knots and use their IRAC colors as probes of the temperature and density in the jets and bowshocks. Such spectra are useful as diagnostics of the C-type shock excitation of pure rotational transitions of  $\text{H}_2$  and a few  $\text{H}_2$  vibrational emissions within each IRAC band. Detailed modeling of the individual shocks will help retrace the history of episodic jet activity and the associated accretion onto the protostar. Our resolution enhanced *Spitzer* image data on such a large sample of protostellar objects will be a resource to future studies of these objects. It is encouraging to see that in addition to our algorithm developed for *Spitzer* images newer ones such as the deconvolution software AWAIC (A *WISE* Astronom-

ical Image Co-Adder) are becoming available. The results presented in this paper support the usefulness and the need for reprocessing with deconvolution techniques the protostellar data obtained by high sensitivity but low spatial resolution observations in *Spitzer*, *Herschel*, and *WISE* surveys.

We acknowledge Dr C. A. Beichman for suggesting the development of the HiRes deconvolution tool for Spitzer images. We also thank the referee for helpful suggestions. This publication makes use of the Protostars Webpage hosted by the University of Kent. This ADAP (ROSES 2009)-sponsored research was conducted at the Jet Propulsion Laboratory, California Institute of Technology under contract with the National Aeronautics and Space Administration. In 1997 the Owens Valley Radio Observatory millimeter array, which we used to observe CO, was supported by the National Science Foundation grant number AST-96-13717 ©2013. All rights reserved. California Institute of Technology: USA Government sponsorship acknowledged.

## REFERENCES

- Arce, H. G., & Sargent, A. I. 2006, *ApJ*, 646, 1070
- Arce, H. G., Mardones, D., Corder, S. A., Garay, G., Noriega-Crespo, A., Raga, A. C. 2013, *ApJ* 774, 39
- Arce, H. G., Shepherd, D., Gueth, F., Lee, C.-F., Bachiller, R., Rosen, A., & Beuther, H. 2007, in *Protostars and Planets V*, p2245
- Aumann, H. H., Fowler, J. W. & Melnyk, M. 1990, *AJ*, 99, 1674
- Backus, C. R., Velusamy, T., Thompson, T. J., & Arballo, J. K. 2005, in *ADASS XIV*, ASP Conference Series, Vol. 347, p 61; P. L. Shopbell, M. C. Britton, and R. Ebert, eds.
- Bally, J. 2007, *Astrophysics & Space Science*, 311, 15
- Bally, J., Devine, D., & Reipurth, B. 1996, *ApJ*, 473, L49
- Bourke, T. L. et al. 2006 *ApJ*, 649, L37
- Caratti o Garatti, A., Froebrich, D., Eisloffel, J., Giannini, T., & Nisini, B. 2008, *A&A*, 485, 137
- Chen, X., Launhardt, R., Bourke, T. L., Henning, Th., & Barnes, P. J. 2008, *ApJ*, 683, 862
- Chen, X., et al. 2013, 768, 110
- Choi, M. 2009, *ApJ*, 705, 1730
- Choi, M., Hodapp, K. W., Hayashi, M., Motohara, K., Pak, S., & Pyo, T.-S. 2006, *ApJ*, 646, 1050
- Connelley, M. S., Reipurth, B., & Tokunaga, A. T. 2008, *AJ*, 135, 2496
- Dionatos, O., Nisini, B., Cabrit, S., Kristensen, L., & Pineau des Forts, G. 2010, *A&A* 521, A7
- Emerson, J. P., Harris, S., Jennings, R. E., Beichman, C. A., Baud, B., Beintema, D. A., Wesselius, P. R., & Marsden, P. L. 1984, *ApJ*, 278, L49
- Enoch, M. L., Corder, S., Dunham, M. M., & Duchene, G. 2009a, *ApJ*, 707, 103
- Fischer, W. J., et al. 2010, *A&A*, 518, L122

- Forbrich, J., et al. 2010, 716, 1453
- Froebrich, D. 2005, ApJS, 156, 169
- Girart, J.M., Rao, R., & Estalella, R. 2009, ApJ 694, 56
- Lee, C.-F., Hasegawa, T. I., Hirano, N., et al. 2010, ApJ, 713, 731
- Ladd, E. F., Fuller, G. A., Deane, J. R. 1998, ApJ, 495, 871
- Launhardt, R., Pavlyuchenkov, Ya., Gueth, F., Chen, X., Dutrey, A., Guilloteau, S., Henning, Th., Pitu, V., Schreyer, K., Semenov, D. 2008, A&A ,494. 147L
- Lucy, L. B. 1974 AJ, 79, 745
- Machida, M. N., Inutsuka, S-I., & Mastumoto, T. 2008, ApJ, 676, 1088
- Masci, F., & Fowler, J. W. 2009, in ASP Conf. Ser. 411, Astronomical Data Analysis Software and Systems XVIII, ed. D. A. Bohlender, D. Durand, & P. Dowler (San Francisco, CA: ASP), 67
- Massi, F., Codella, C., & Brand, J. 2004, A&A, 419, 241
- Miettinen, O. & Offner, S. S. R. 2013, A&A, 553, A88
- Moro-Martín, A., Noriega-Crespo, A., Molinari, S., et al. 2001, ApJ, 555, 146
- Mundt, R. & Fried, J. W. 1983, ApJ, 274, L83
- Neufeld, D. A. & Yuan, Y. 2008, ApJ, 678, 974
- Noriega-Crespo, A., et al. 2004a, ApJS, 154, 352
- Noriega-Crespo, A., et al. 2004b, ApJS, 154, 402
- Noriega-Crespo, A. & Raga, A. C. 2012, ApJ, 750, 501
- Offner, S. S. R., Lee, E. J., Goodman, A. A., & Arce, H. 2011, ApJ, 743, 91
- Pudritz, R. E., Ouyed, R., Fendt, Ch., & Brandenburg, A. 2007, in Protostars and Planets V, p277
- Raga, A. C., Barnes, P. J., & Mateo, M. 1990, AJ, 99, 1912
- Reipurth, B., Heathcote, S., Roth, M., Noriega-Crespo, A., & Raga, A. C. 1993, ApJ, 408, 49

- Reipurth, B. & Heathcote, S. 1992, *A&A*, 257, 693
- Richardson, W. H. 1972 *J. Opt. Soc. Am.*, 62, 55
- Robitaille, T. P., Whitney, B. A., Indebetouw, R., & Wood, K. 2007, *ApJS*, 169, 328
- Seale, J. P., & Looney, L. W. 2008, *ApJ*, 675, 427
- Shepherd, D. S., Yu K. C., Bally J., & Testi L. 2000, *Astrophys.J.*, 535, 833-846.
- Smith, M. D., & Rosen, A. 2005, *MNRAS*, 357, 1370
- Stecklum, B., Launhardt, R., Fischer, O., Henden, A., Leinert, C., & Meusinger, H. 2004, *ApJ*, 617, 418
- Stutz, A. M., Rubin, M., Werner, M. W., Rieke, G. H., Bieging, J. H., Keene, J., Kang, M., Shirley, Y. L., Su, K. Y. L., Velusamy, & T., Wilner, D. J. 2008, *ApJ*, 687, 389
- Shu, F. H., Najita, J. R., Shang, H., & Li, Z.-Y. 2000, in *Protostars and Planets IV*, ed. V. Mannings, A. P. Boss, & S. S. Russell (Tucson: Univ. Arizona Press), 789
- Takakuwa, S., Ohashi, N., Bourke, T. L., Hirano, N., Ho, P. T. P., Jrgensen, J. K., Kuan, Y., Wilner, D. J., Yeh, S. C. 2007, *ApJ* 662, 431
- Tobin, J. J., Looney, L. W., Mundy, L. G., Kwon, W., & Hamidouche, M. 2007, *ApJ*. 659, 1404
- Tobin, J. J., Hartmann, L., Calvet, N., & DAlessio, P. 2008, *ApJ*, 679, 1364
- Tobin, J. J., Hartmann, L., & Loinard, L. 2010, *ApJL*, 722, L12
- Velusamy, T. & Langer, W. D. 1998, *Nature* 392, 686
- Velusamy, T., Langer, W. D., Marsh, K. A. 2007 *ApJL*, 668, L159
- Velusamy, T., Marsh, K. A., Beichman, C. A., Backus, C. R., & Thompson, T. J. 2008, *AJ* 139, 197
- Velusamy, T., Langer, W. D., Kumar, M. S. N., & Grave, J. M. C. 2011, *ApJ*, 741, 60
- Wu, Y., Wei, Y.; Zhao, M., Shi, Y., Yu, W.; Qin, S., & Huang, M. 2004, *A&A*, 426, 503
- Ybarra, J. E., & Lada, E. A. 2009, *ApJL*, 695, L123
- Yu, K. C., Billawala, Y., & Bally, J. 1999, *AJ*, 118, 2940



Table 1: **List of protostars, jets and outflows in the *Spitzer* HiRes processed sample**

No.	Primary Name	Other/ Region	RA (2000)	Dec. (2000)	Ref	Data <sup>†</sup>	Fig. No.
1	HH 1-2 MMS 3	L1641	05 36 18.2	-06 45 45.3	1,2	bcd	3.1
2	HH 1-2 MMS 2	L1641	05 36 18.8	-06 45 25.3	1,2	bcd	3.1
3	L 1641 VLA1	HH1-2 VLA	05 36 22.8	-06 46 07.6	1,2	bcd	3.1
4	HH 144	L1641	05 36 21.2	-06 46 07	2,3	bcd	3.1
5	HH 147 MMS	IRAS 05339-0646	05 36 25.2	-06 44 39.8	1	bcd	3.1
6	L 1448-IRS2	L1448	03 25 22.5	+30 45 06	1	bcd	3.2
7	L 1448 NW	L1448	03 25 35.6	+30 45 34	1	bcd	3.3
8	L 1448 N IRS 3B	L1448	03 25 36.3	+30 45 15	1	bcd	3.3
9	L 1448 N IRS 3A	L1448	03 25 36.5	+30 45 22	1	bcd	3.3
10	L 1448 C (N)	L1448	03 25 38.9	+30 44 06	1	bcd	3.3
11	L 1448 C (S)	L1448	03 25 39.1	+30 43 59	1	bcd	3.3
12	NGC 1333 I1	IRAS03255+3103	03 28 38.7	+31 13 32	1	bcd	3.4
13	IRAS 03256+3055	NGC1333/Bolo 33	03 28 44.5	+31 05 39.7	1,4	bcd	3.5
14	NGC 1333-I2 IRAS 2A	IRAS 03258+3104	03 28 55.59	+31 14 37.3	1,5	bcd	3.6
15	NGC 1333-I2 IRAS 2B	NGC1333	03 28 57.21	+31 14 19.1	1,5	bcd	3.6
16	HH 12	NGC1333 I6	03 29 01	+31 20 21	1,5	bcd	3.7
17	HRF 46	NGC1333	03 29 10.82	+31 18 19.5	1	bcd	3.8
18	HH 6	NGC1333 I7	03 29 13	+31 18 41	5	bcd	3.8
19	HRF 65	NGC1333	03 29 00.51	+31 12 00.6	1	pbcd	3.9
20	HH 344 A/B	NGC1333	03 29 00.51	+31 13 38	5	pbcd	3.9
21	HL 3-8	NGC1333	03 29 06	+31 12 00.6	9	pbcd	3.10
22	HH 7-11	NGC1333	03 29 03.06	+31 15 51.7	5	pbcd	3.11
23	SVS 13 B MMS3	NGC1333 I13C	03 29 01.95	+31 15 38.3	1	pbcd	3.11
24	SVS 13 B MMS2	NGC1333 I13B	03 29 03.06	+31 15 51.7	1	pbcd	3.11
25	SVS 13 B MMS1	NGC1333 I13	03 29 03.76	+31 16 04.0	1	pbcd	3.11
26	HH 7-11 MMS6	NGC1333	03 29 04.00	+31 14 46.7	1	pbcd	3.9
27	NGC 1333-I4 A2	NGC1333	03 29 10.42	+31 13 32.2	1,6	pbcd	3.10
28	NGC 1333-I4 A1	NGC1333	03 29 10.53	+31 13 31.1	1,6	pbcd	3.10
29	NGC 1333-I4 B	NGC1333	03 29 13.6	+31 13 06.6	1,6	pbcd	3.10
30	NGC 1333-I4C	NGC1333	03 29 13.62	+31 13 57.9	1,6	pbcd	3.10
31	ASR 57	NGC1333	03 29 14.5	+31 14 44	6	pbcd	3.12
32	HH 347 A/B	NGC1333	03 29 14.5	+31 14 44	5	pbcd	3.12
33	HH 5 A/B	NGC1333	03 29 20	+31 12 48	5	pbcd	3.13
34	IRAS 03282+3035	NGC1333	03 31 20.3	+30 45 25	1	pbcd	3.14
35	Bolo 102		03 43 51.1	+32 03 23	1,3	bcd	3.15

Table 1: **continued**

No.	Primary Name	Other/ Region	RA (2000)	Dec. (2000)	Ref	Data <sup>†</sup>	Fig. No.
36	HH 211 MMS		03 43 56	+32 00 48.0	1	bcd	3.16
37	IC 348 MMS		03:43:57.2	32:03:05	1	bcd	3.17
38	B 5-IRS1	B5	03 47 41.6	+32 51 43	7	bcd	3.18
39	B 213	IRAS04166+2706	04 19 42.6	27 13 38	1	pbcd	3.19
40	L 1551-IRS 5	IRAS 04287+1801	04 31 34.15	+18 08 05.2	1	bcd	3.20
41	L 1551-NE A/B		04 31 44.47	+18 08 31.9	1	bcd	3.21
42	IRAS 04325+2402	L 1535 IRS	04 35 35.0	+24 08 22	1	pbcd	3.22
43	L 1527	IRAS 04368+2557	04 39 53.9	+26 03 11	1	bcd	3.23
44	CB 26	L 1429	04 59 50.74	52 04 43.8	9	pbcd	3.24
45	L 1634 IRS 7		05 19 51.5	-05 52 06	1	pbcd	3.25
46	IRAS 05173-0555	L 1634	05 19 48.9	-05 52 05	1	pbcd	3.25
47	Haro-4-357	MHO 81	05 35 15	-06 13 40	10	bcd	3.26
48	Haro-4-352	MHO 117, HH40	05 35 21	-06 18 23	10	bcd	3.27
49	HH 34		05 35 30	-06 26 58	11	bcd	3.28
50	L 1641-N		05 36 18.6	-06 22 10	1	bcd	3.29
51	L 1641 SMS III		05 36 24.0	-06 24 54	1	bcd	3.29
52	HH 92	IRAS 05399-0121	05 42 28	-01 20 01	7	bcd	3.30
53	HH 212-MM		05 43 51.1	-01 03 01	1	bcd	3.31
54	HH 25 MMS		05 46 07.8	-00 13 41	1	bcd	3.32
55	HH 26 IR		05 46 05.4	-00 14 16.6	8	bcd	3.32
56	HH 24 MMS		05 46 08.8	-00 10 47	1	bcd	3.33
57	HH 111 MMS		05 51 46.3	+02 48 28	1	bcd	3.34
58	NGC 2264 G-VLA 2		06 41 10.9	+09 56 02	1	bcd	3.35
59	CG 30-N/ BHR12	IRAS 08076-3556	08 09 33.1	-36 04 58.1	1,12	pbcd	3.36
60	CG 30-S	IRAS 08076-3556	08 09 32.7	-36 05 19.1	1,12	pbcd	3.36
61	HH 46/47		08 25 43	-51 00 36	13	bcd	3.37
62	BHR 71 IRS1	IRAS 11590-6452	12 01 36.8	-65 08 49	1,12	pbcd	3.38
63	BHR 71 IRS2	IRAS 11590-6452	12 01 34.1	-65 08 47	1,12	pbcd	3.38
64	IRAS 15398-3359		15 43 01.3	-34 09 12	1	pbcd	3.39
65	IRAS 16293-2422 A/B		16 32 22.62	-24 28 32.3	1	pbcd	3.40
66	L 483	IRAS 18148-0440	18 17 29.8	-04 39 38.3	1	bcd	3.41
67	Serp-FIRS1(SMM1)	IRAS 18273+0113	18 29 49.80	01 15 20.6	1,17	pbcd	3.42
68	Serp-S68N		18 29 48.1	01 16 41	1	pbcd	3.42
69	Serp-SMM5		18 29 51.1	01 16 36	1	pbcd	3.42
70	Serp-SMM10		18 29 52.1	01 15 48	1	pbcd	3.42

Table 1: **continued**

No.	Primary Name	Other/ Region	RA (2000)	Dec. (2000)	Ref	Data <sup>†</sup>	Fig. No.
71	L 723	HH223	19 17 53.16	+19 12 16.6	1	pbcd	3.43
72	B 335	IRAS 19345+0727	19 37 01.03	+07 34 10.9	1	bcd	3.44
73	IRAS 20126+4104		20 14 26.0	+41 13 32	14	pbcd	3.45
74	L1152	IRAS 20353+6742	20 35 45.9	+67 53 02	1	pbcd	3.46
75	L 1157	IRAS 20386+6751	20 39 06.5	+68 02 13	1	bcd	3.47
76	L 1228		20 57 13.00	+77 35 43.6	1	bcd	3.48
77	CB 230 A	IRAS 21169+6804	21 17 38.5	+68 17 33.0	1,15	pbcd	3.49
78	CB 230 B	IRAS 21169+6805	21 17 40.3	+68 17 32.7	1,15	pbcd	3.49
79	L 1251B IRS4		22 38 42.80	+75 11 36.8	1	pbcd	3.50
80	L 1251B IRS1		22 38 46.9	+75 11 33.9	1	pbcd	3.50
81	L 1251 B		22 38 47.2	+75 11 28.8	1	pbcd	3.50
82	L 1251B IRS2		22 38 53.0	+75 11 23.5	1	pbcd	3.50
83	L 1251B 16		22 39 13.3	+75 12 15.8	1	pbcd	3.51
84	L 1211 MMS1		22 47 02.2	+62 01 32	1	pbcd	3.51
85	L 1211 MMS2		22 47 07.6	+62 01 26	1	pbcd	3.51
86	L 1211 MMS3		22 47 12.4	+62 01 37	1	pbcd	3.51
87	L 1211 MMS4		22 47 17.2	+62 02 34	1	pbcd	3.51
88	Cep E-MM		23 03 13.1	+61 42 26	1	bcd	3.52
89	IRAS 23238+7401		23 25 46.4	+74 17 38	16	pbcd	3.53

<sup>†</sup>The terms bcd and pbcd refer to the BCD and post-BCD data from *Spitzer* archives which were used for HiRes deconvolution (see text).

References: (1) The Youngest Protostars Webpage: <http://astro.kent.ac.uk/protostars/old/>; (2) Noriega-crespo & Raga 2012 ; (3) Reipurth et al. 1993; (4) Enoch et al. 2009; (5) Bally et al. 1996; (6) Choi et al. 2006; (7) Connellley et al. 2008; (8) Wu et al. 2004; (9) Launhardt et al. 2008; (10) MHO catalog: <http://www.astro.ljmu.ac.uk/MHCat/>; (11) Reipurth et al. 1992; (12) Chen et al. 2008; (13) Noriega-crespo et al. 2004; (14) Caratti o Garatti et al. 2008; (15) Massi et al. 2004; (16) Seale & Looney 2008; (17) Choi 2009

Table 2: **Opening Angle of Wide Angle Outflow Cavities**

Primary Name	Opening angle(deg) <sup>†</sup>	T <sub>bol</sub> (K)	ref.	age <sup>‡</sup> 10 <sup>3</sup> yr
L1641 VLA1	50	41	1	0.9 ( 0.2 , 3.7 )
L 1448-IRS2	70	43-63	2	2.6 ( 0.7 , 10.4 )
L 1448 C (N)	65	49-69	2	3.3 ( 0.8 , 13.0 )
HH12	100	304	2	115 ( 29 , 456 )
IRAS 03256+3055	100	67	2	3.0 ( 0.8 , 12.1 )
IRAS03282+3035	80	33-60	3	1.3 ( 0.3 , 5.2 )
Bolo 102	95	72	2	3.6 ( 0.9 , 14.4 )
HH 211-MM	50	24	2	0.3 ( 0.1 , 1.0 )
B5 IRS1	130	287	2	100 ( 25 , 397 )
B213	80	72	2	3.6 ( 0.9 , 14.4 )
L 1551-IRS 5	105	92	4	6.5 ( 1.6 , 25.9 )
L 1551-NE A/B	100	91	4	6.3 ( 1.6 , 25.2 )
IRAS 04325+2402	110	73	4	3.7 ( 0.9 , 14.9 )
L1527	98	56	4	2.0 ( 0.5 , 7.9 )
CB26	115	770	5	1065 ( 268 , 4242 )
L 1634 IRS7	76	64*	6	2.7 ( 0.7 , 10.8 )
IRAS05173-0555	64	58*	6	5.7 ( 1.4 , 22.6 )
HH92	60	41*	7	0.9 ( 0.2 , 3.7 )
HH111MMS	118	78	4	4.4 ( 1.1 , 17.4 )
IRAS08076-3556	42	117	4	0.7 ( 0.2 , 2.9 )
HH46/47	110	40-145	8	19.4 ( 4.9 , 77.1 )
BHR71-IRS1	45	44	9	1.1 ( 0.3 , 4.4 )
BHR71-IRS2	42	58	9	2.1 ( 0.5 , 8.6 )
IRAS15398-3359	120	48-61	4	2.4 ( 0.6 , 9.7 )
L483	70	50-54	3	1.8 ( 0.5 , 7.2 )
B335	63	28-45	3	1.2 ( 0.3 , 4.7 )
L1152	64	48*	6	1.4 ( 0.3 , 5.4 )
L1157	54	40-60	3	1.0 ( 0.2 , 3.9 )
CB230	95	69	4	3.3 ( 0.8 , 13.0 )
CepE-MM	85	56	4	2.0 ( 0.5 , 7.9 )
IRAS23238+7401	98	64*	6	2.7 ( 0.7 , 10.8 )

<sup>†</sup>This paper

<sup>‡</sup>1- $\sigma$  lower and upper limits are given in parenthesis

\*Estimated from SED peak.

References for T<sub>bol</sub>: (1) Fischer et al. 2010; (2) Enoch et al. 2009; (3) Chen et al. 2013; (4) Froebrich 2005; (5) Stecklum et al. 2004; (6) Seale & Looney 2008; (7) Miettinen et al.2013; (8) Emerson et al. 1994; (9) Chen et al. 2008.

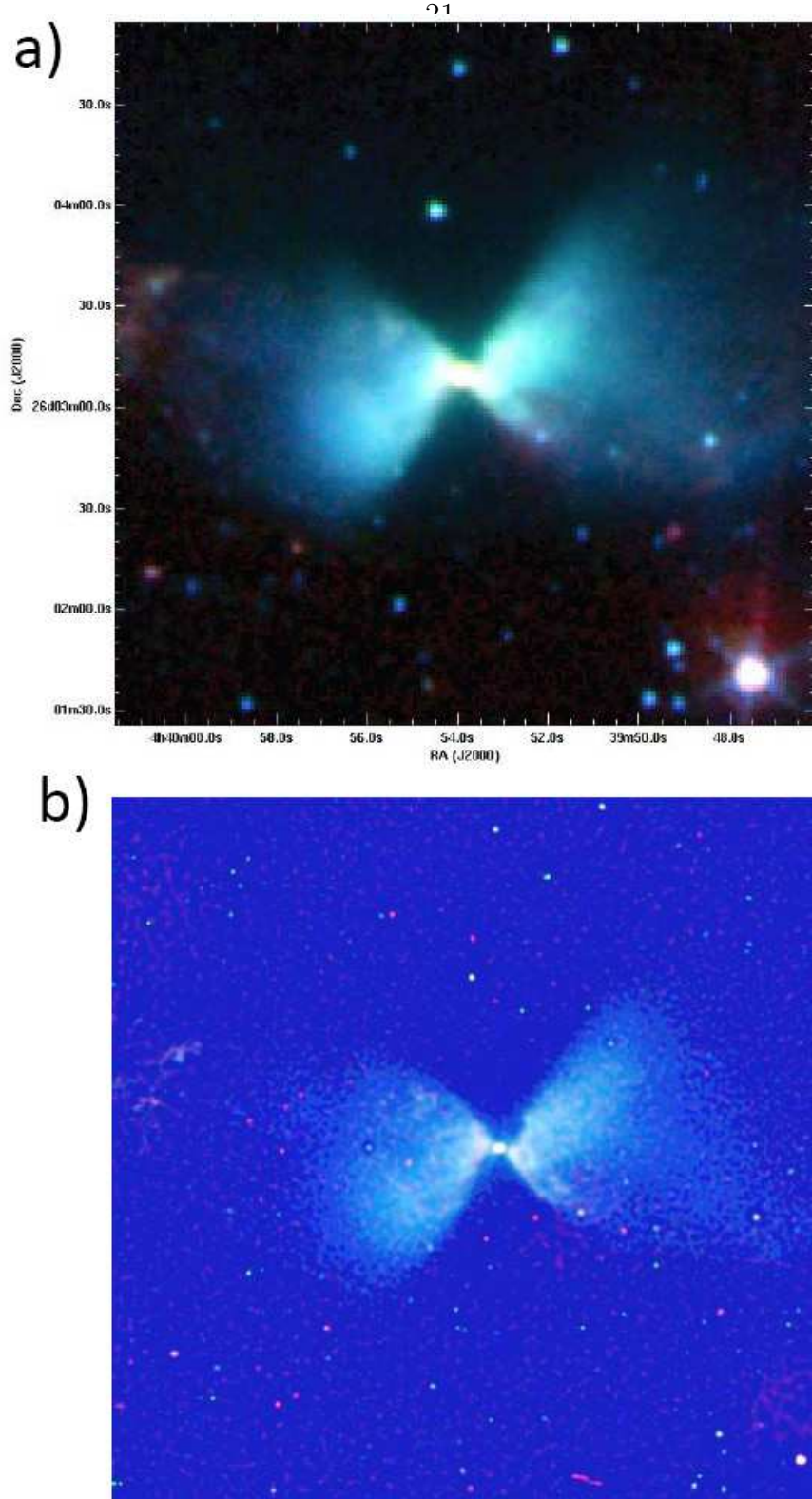


Fig. 1.— Example of a comparison of HiRes denconvolved *Spitzer* IRAC images with unprocessed mosaic images in the literature: false 3-color IRAC images of L1527 (blue:  $3.6\ \mu\text{m}$ ; green:  $4.5\ \mu\text{m}$ ; and red:  $8.0\ \mu\text{m}$ ). (a) unprocessed mosaic image reproduced from Tobin et al. (2008). (b) the HiRes deconvolved image.

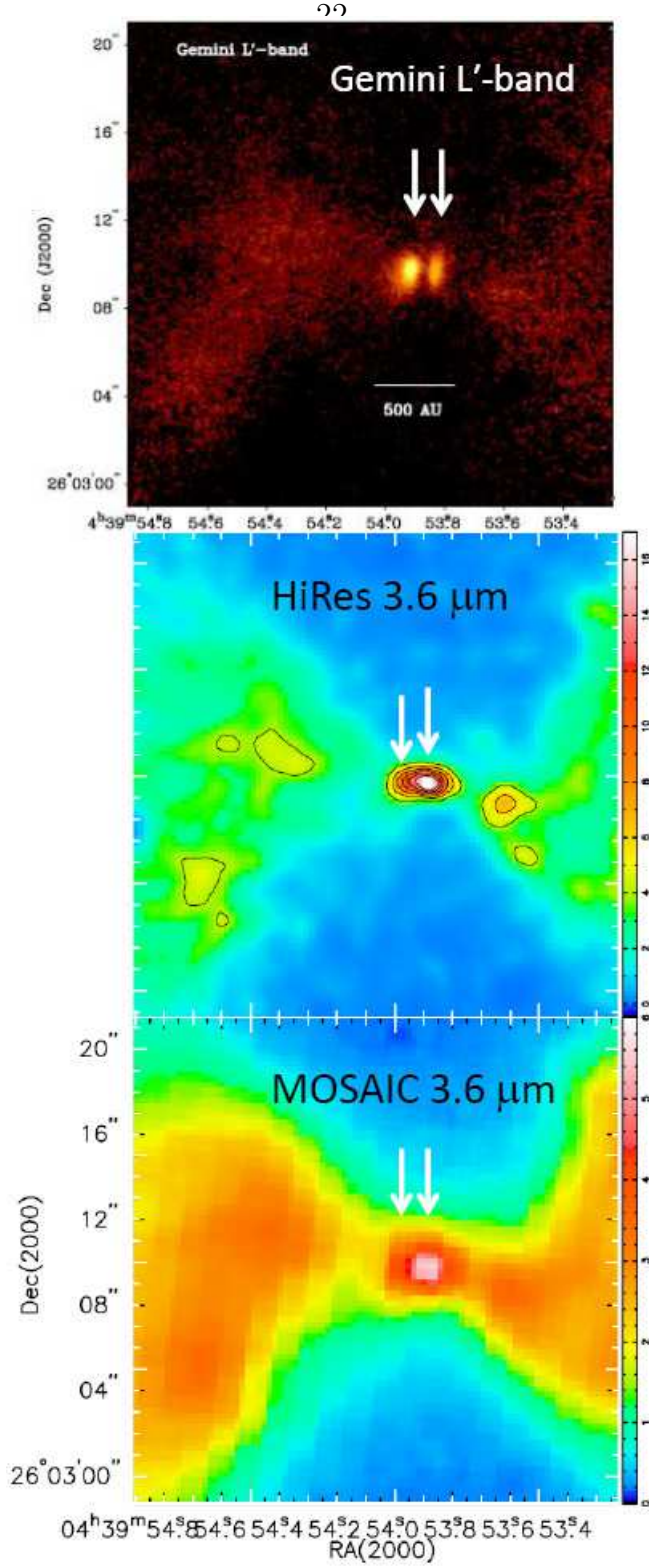


Fig. 2.— *Spitzer* 3.6  $\mu\text{m}$  HiRes deconvolved image compared with high resolution (with a pixel scale of 0.049") Gemini L' - band (3.8  $\mu\text{m}$ ) image of the outflow in L1527. For comparison the IRAC 3.6  $\mu\text{m}$  mosaic image is shown in the lower panel. Note the sub-arcsec resolution enhancement in the deconvolved image (middle panel) brings out the innermost structure as observed in the high resolution image in the top panel (reproduced from Tobin et al. 2010).



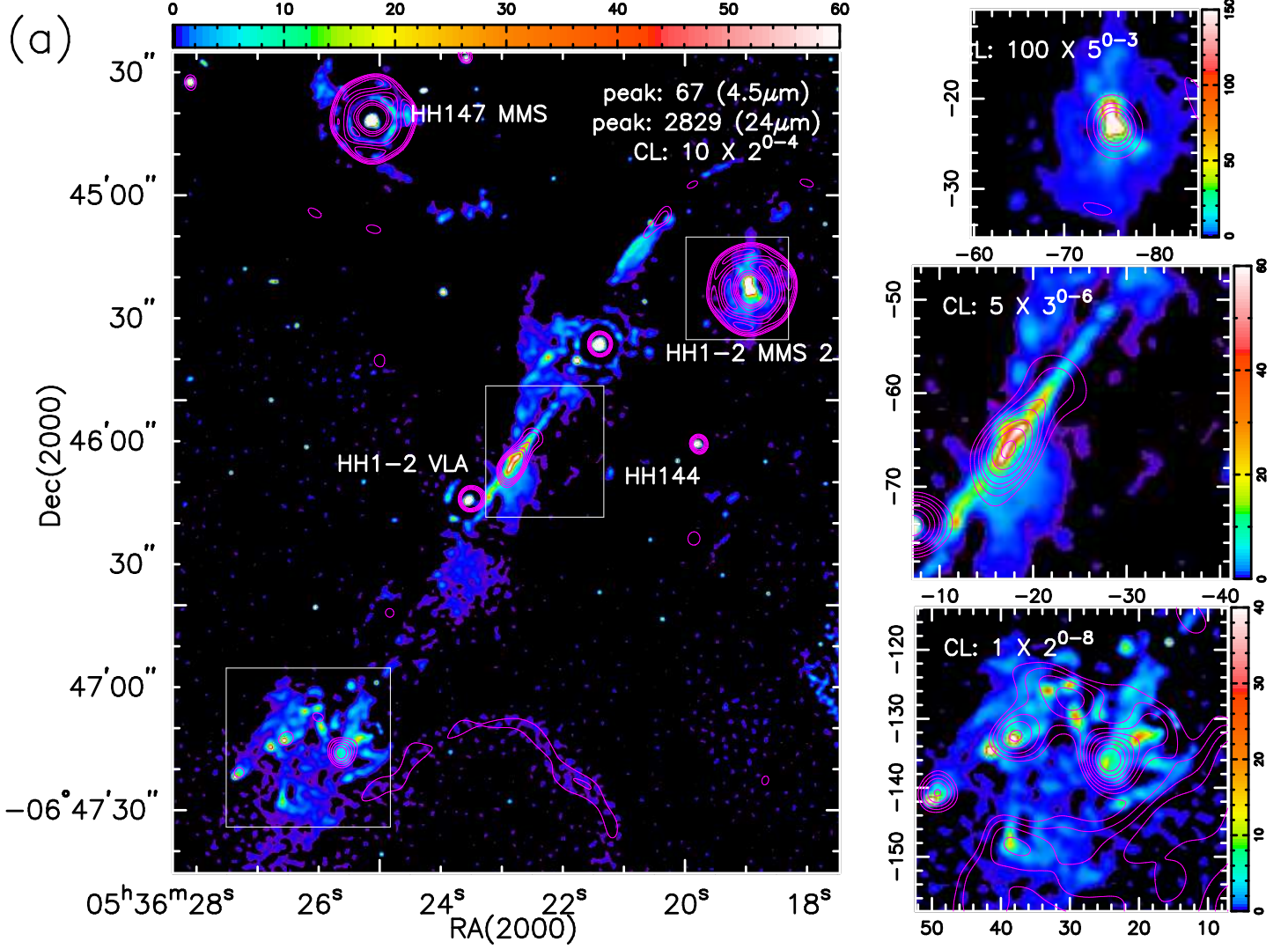


Fig. 3.1a.— HH1-2: The HiRes MIPS  $24\mu\text{m}$  image overlaid as contours on the IRAC  $4.5\mu\text{m}$  image. For details see caption for FIGURE SET 3 below.

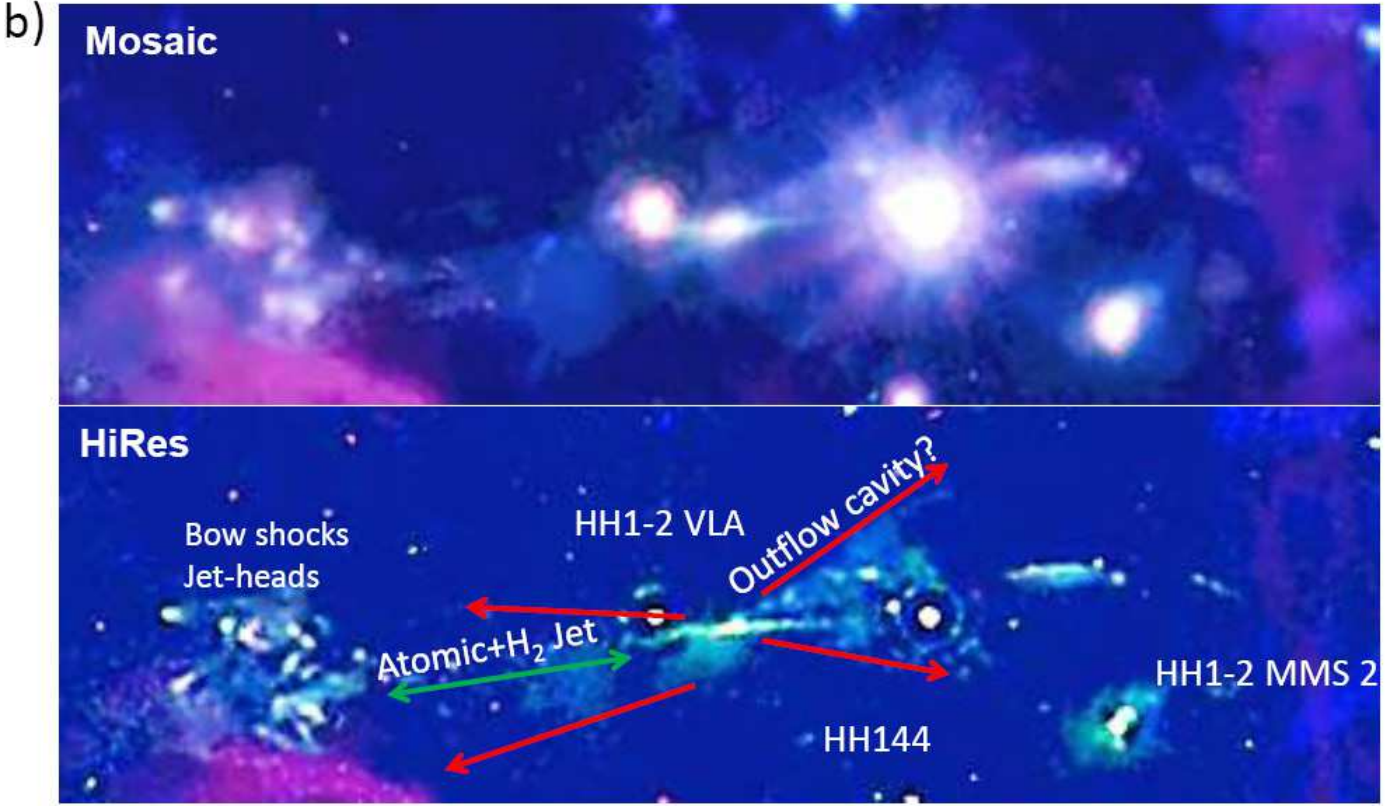


Fig. 3.1b.— HH1-2: 3-color mosaic and HiRes images:  $3.6\ \mu\text{m}$  (blue),  $4.5\ \mu\text{m}$  (green),  $8.0\ \mu\text{m}$  (red). For details see caption for FIGURE SET 3 below.

FIGURE SET 3: See the electronic edition of the Journal for all 53 images.

Caption to **Figures 3.1 to 3.53**: (a) The  $4.5\ \mu\text{m}$  and  $24\ \mu\text{m}$  HiRes deconvolved *Spitzer* IRAC image of the protostellar jet and outflow in our sample. The MIPS  $24\ \mu\text{m}$  image overlaid as contours on the IRAC  $4.5\ \mu\text{m}$  gray scale image (in a few cases the  $3.6\ \mu\text{m}$  image is used and is indicated in the image). A square root color stretch is used to bring out low and high brightness emissions and the contour levels are in increments of factors of two or larger as indicated. The peak intensities (in units of  $\text{MJy Sr}^{-1}$ ) in the protostar/jet-outflow are indicated. The panels to the right show blowups of the selected regions (indicated by the boxes in the left panel) where it is needed to bring out the features. In some cases the positions of the resolved stellar components in the IRAC and  $8.0\ \mu\text{m}$  images are labeled. In cases where the atomic jet features, traced by the atomic and/or ionic line emissions within the MIPS  $24\ \mu\text{m}$  band are present they are identified by the  $24\ \mu\text{m}$  contours overlaid on  $4.5\ \mu\text{m}$  gray scale image. (b) 3-color representation of HiRes deconvolved *Spitzer* IRAC images: IRAC  $3.6\ \mu\text{m}$  (blue),  $4.5\ \mu\text{m}$  (green),  $8.0\ \mu\text{m}$  (red). In some cases the arrows (white) or numbers mark positions of the resolved stellar components in the IRAC  $5.8$  and  $8.0\ \mu\text{m}$  images. The images are re-orientated to conserve space and the orientation in the sky is easily inferred from the image in the upper panel. Muxbleed artifacts if present are indicated by a cross. In the 3-color representation the wide angle outflows are identified by the blue excess while the  $\text{H}_2$  jets and bow shocks by the green excess. The  $\text{H}_2$  jets (green arrows) and the wide angle cavity (red arrows) inferred from scattered light are indicated (not to scale).





Fig. 4.— Image gallery of wide angle outflows observed in the HiRes processed *Spitzer* sample: 3-color IRAC HiRes image with  $3.6\ \mu\text{m}$  (blue),  $4.5\ \mu\text{m}$  (green), and  $8.0\ \mu\text{m}$  (red). The wide angle cavities are identified by the color excess (blue). Note B5 IRS1 and HH12 have large side-lobe residue due to saturation.



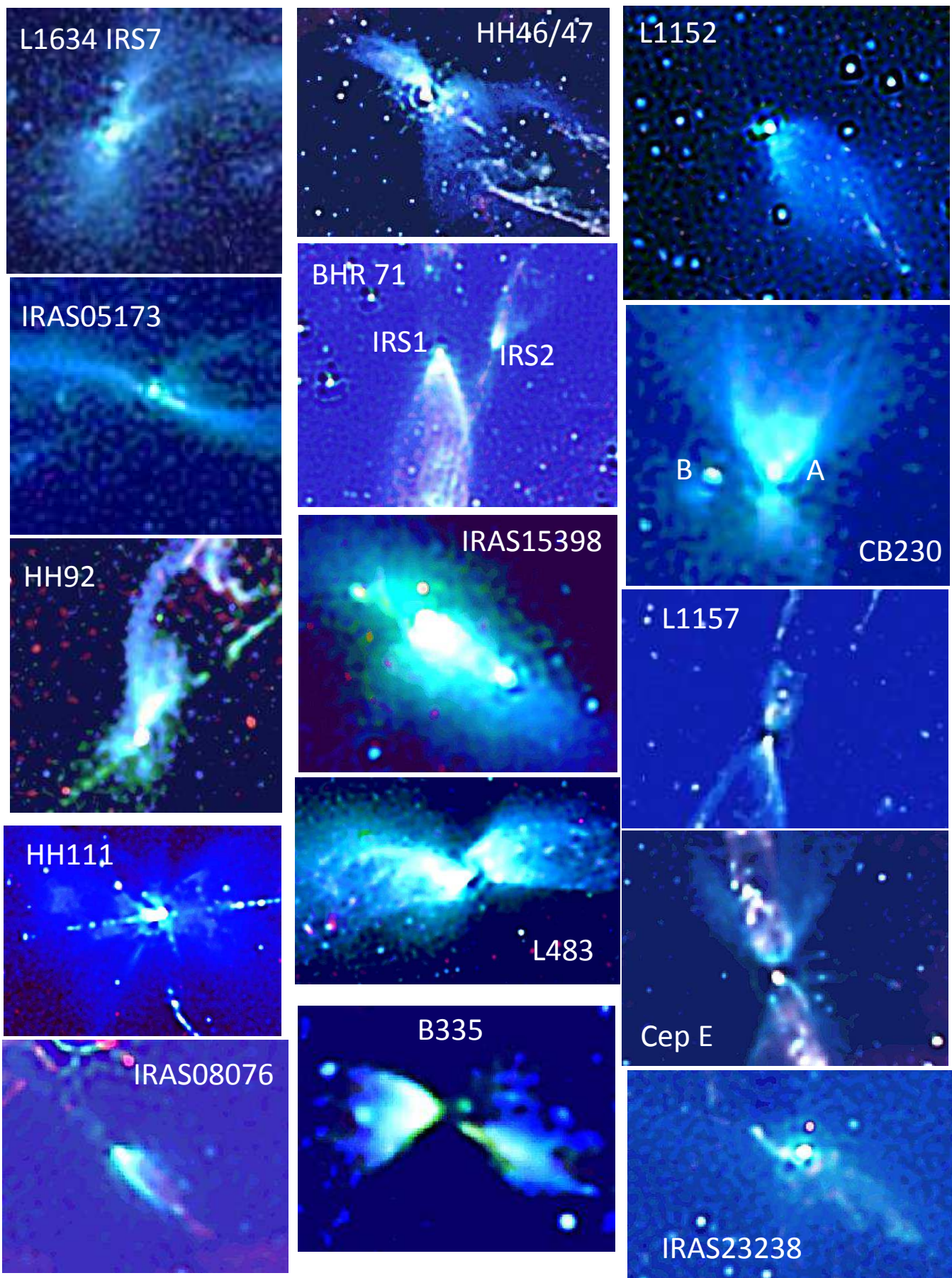


Fig. 4.— (Continued)

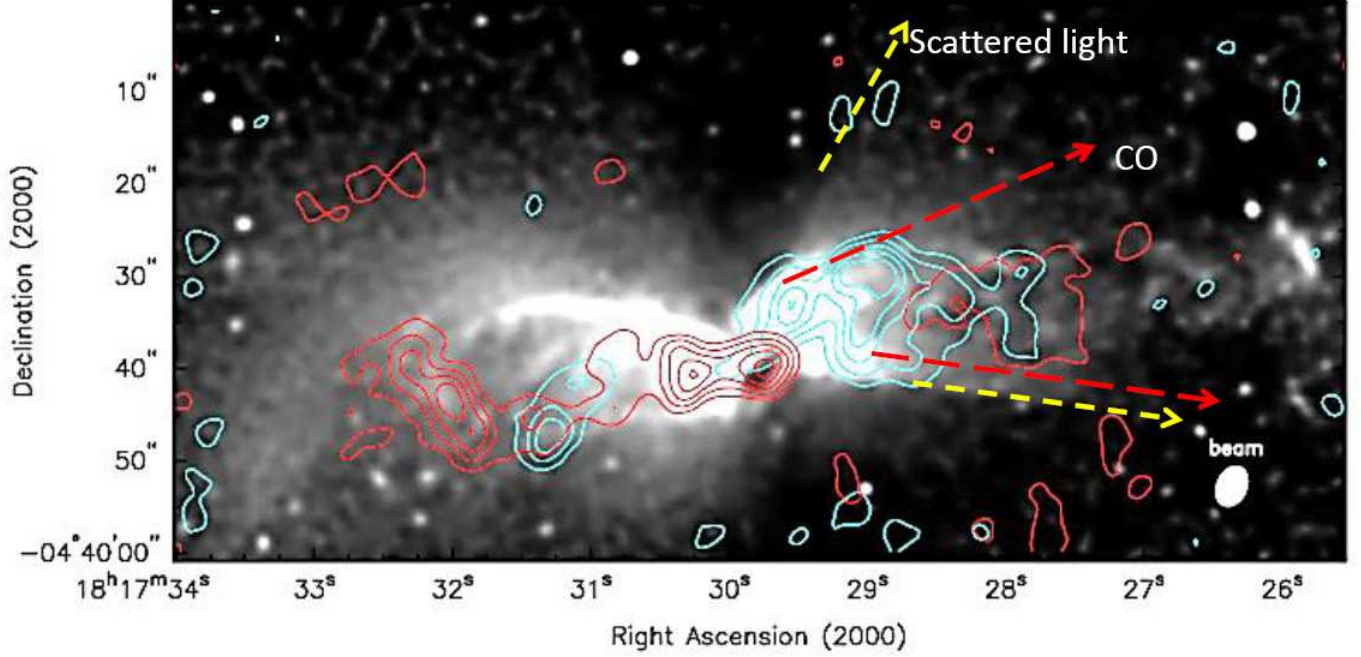


Fig. 5.— L483: Comparison of the scattered light outflow cavity traced in HiRes 4.5  $\mu\text{m}$  image with  $^{12}\text{CO}(1-0)$  outflow lobes. CO outflow intensity contours (at interval 0.4 Jy  $\text{beam}^{-1}$ ) overlaid on the 4.5  $\mu\text{m}$  image. Red and blue contours represent the red-shifted ( $V_{lsr}$  6.5 – 10.4  $\text{km s}^{-1}$ ) and blue-shifted ( $V_{lsr}$  0.0 – 3.9  $\text{km s}^{-1}$ ) lobes respectively. The rest  $V_{lsr}$  is 5.2  $\text{km s}^{-1}$ . The CO data are from our OVRO observations with a synthesized beam of 4.6''  $\times$  3.3''. The arrows mark the outflow cavities as traced by the scattered light at 4.5  $\mu\text{m}$  and CO emissions.

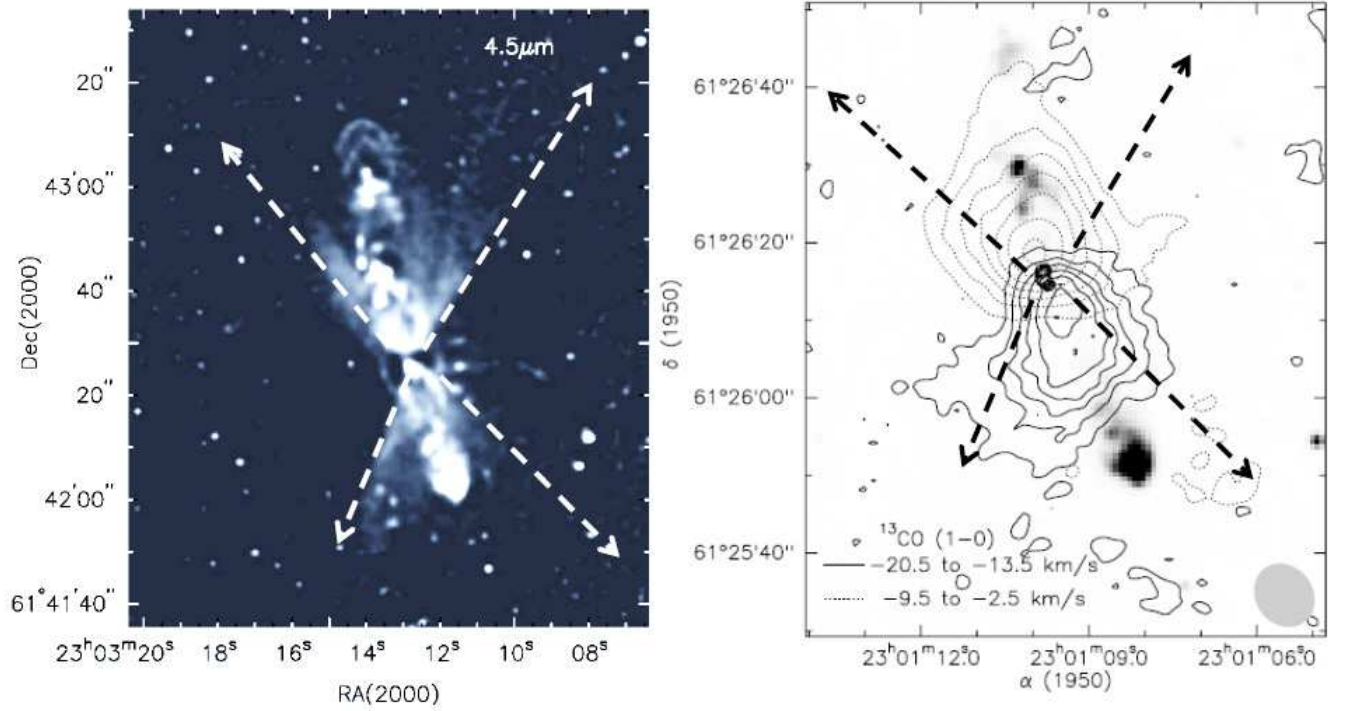


Fig. 6.— Cep E: Comparison of the scattered light outflow cavity traced in the HiRes  $4.5 \mu\text{m}$  image with  $^{13}\text{CO}(1-0)$  outflow lobes. (left)  $4.5 \mu\text{m}$  image. (right) Contour map of CO outflow intensities of the red-shifted and blue-shifted lobes observed with the OVRO (reproduced from Moro-Martín et al. 2001). The arrows mark the outflow cavity traced by the scattered light at  $4.5 \mu\text{m}$ .

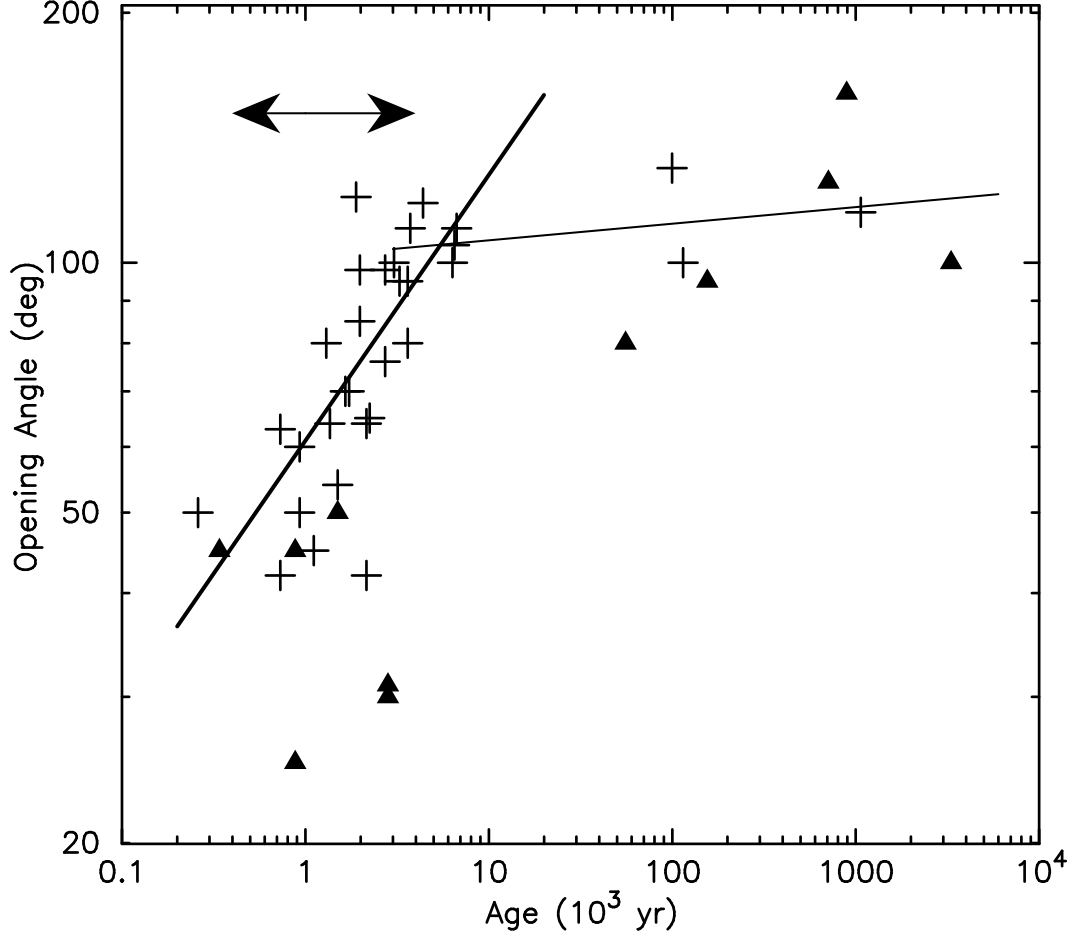


Fig. 7.— Age versus the opening angle of all wide angle outflows detected in the HiRes images. The crosses (+) are data from the present sample, used for the power law fits. The power law fits, for opening angle versus age, are shown for ages  $< 8000$  yr (thick line) and for ages  $> 7000$  yr (thin line) have exponents 0.32 and 0.02 respectively. Filled triangles are data from Arce & Sargent (2006) which are not used for the fit. The double arrow indicates the uncertainty in the age estimate.

Fig. 3.2 to 3.53.— See the electronic edition of January 20, 2014 ApJ V781-1